Experiments in Fluids (2022) 63:17
https://doi.org/10.1007/s00348-021-03370-w

RESEARCH ARTICLE

Study of internal time-resolved flow dynamics of a subsonic fluidic oscillator using fast pressure sensitive paint

Luanliang Zhou[1,2] · Shiqi Wang[3] · Jinsheng Song[1,2] · Ziyan Li[1,2] · Xu Liu[1,2] · Di Peng[1,2] · Xin Wen[1,2] · Yingzheng Liu[1,2]

Received: 7 September 2021 / Revised: 20 November 2021 / Accepted: 13 December 2021 / Published online: 24 December 2021

Abstract

This work applied fast mesoporous-particle-based pressure-sensitive paint (PSP) to obtain the time-resolved flow dynamics inside fluidic oscillators with jet speed up to 0.7 Mach and oscillation frequencies higher than 1 kHz. The frequency of the oscillator decreases as the feedback channel length increases. The frequency characteristics can be divided into a linear growth stage and a slow change stage. The external velocity characteristic of the oscillator also presented a double-peak phenomenon. Pressure wave reflection theory was used to explain the double-peak phenomenon of velocity, which was verified according to the PSP dynamic pressure field. In addition, the proper orthogonal decomposition method was applied to the PSP snapshots to further explain the dominating pressure propagation and small-scale pressure changes.

Graphical Abstract

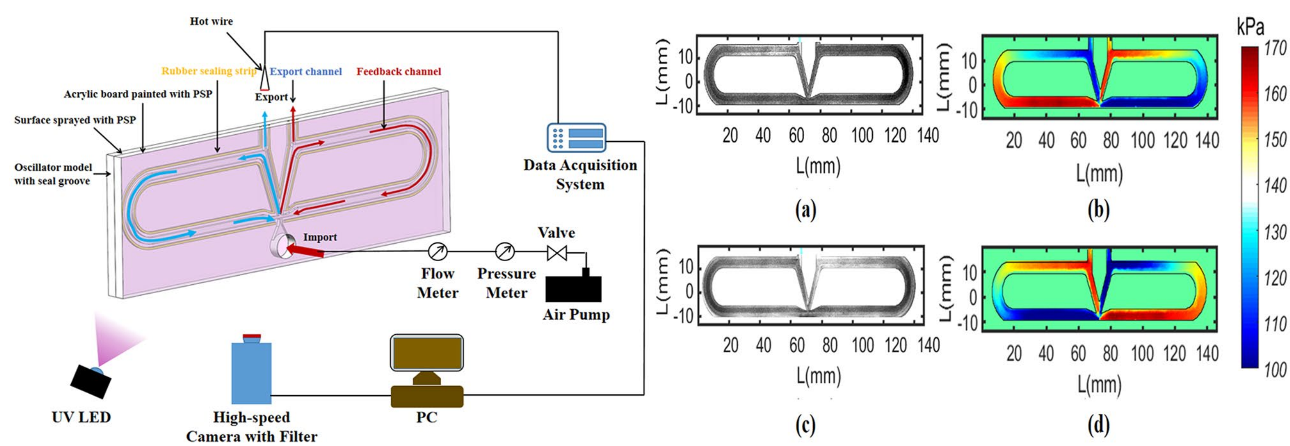

Abbreviations

HPCW	High pressure compression wave
LPEW	Low pressure expansion wave
MP-PSP	Mesoporous-particle-based pressure-sensitive paint
PC-PSP	Polymer-ceramic pressure-sensitive paint
PSP	Pressure-sensitive paint
POD	Proper orthogonal decomposition
Wind-off Average	The average value of 5000 wind-off images
Wind-on Average	The average value of 10,000 wind-on images

List of symbols

L_f	The length of the feedback channel
P_i	Inlet pressure (bar)
U_{max}	The velocity at the outlet of oscillator
U_{max}	The maximum value of velocity at the outlet of oscillator

✉ Xin Wen
wenxin84@sjtu.edu.cn

[1] Key Lab of Education Ministry for Power Machinery and Engineering, Shanghai, China

[2] Gas Turbine Research Institute, Shanghai Jiao Tong University, 800 Dongchuan Road, Shanghai 200240, China

[3] Aero-Engine Academy of China, Beijing 101304, China

U_{min}	The minimum value of velocity at the outlet of oscillator
B_1	The center of the straight channel of the left half of the oscillator
C_1	The entrance of the feedback channel of the left half of the oscillator
C_2	The entrance of the feedback channel of the right half of the oscillator
D_1	The center of the straight channel of the left half of the oscillator
E_1	The exit of the feedback channel of the left half of the oscillator
I_{on}	Intensity of PSP (count)
I_{ref}	Intensity of PSP at reference condition (count)
P_{ref}	Pressure at reference condition (kPa)
t_{C1D1}	The time for the high voltage to propagate from point C_1 to point D_1
t_{C1E1}	The time for the high voltage to propagate from point C_1 to point E_1
t_{C1C2}	The time for the high voltage to propagate from point C_1 to point C_2
L_{C1E1}	The length for the high voltage to propagate from point C_1 to point E_1
U_{C1E1}	The velocity for the high voltage to propagate from point C_1 to point E_1
T_t	The transmission time of the pressure wave in the feedback channel on one side
T_s	The deflection time of the main jet to overcome the wall effect
c	Velocity of sound
St	Stanton number (fL_f/U_{C1E1})
P_1	The increased pressure at point C_1 is affected by the reflected high wave
P_2	The value of pressure of C_1 is higher than that of B_1 when B_1 and C_1 both reach the highest point
P_3	The difference between the lowest value of the pressure at point E_1 and the lowest value of the pressure in the feedback channel
P_4	The increased pressure at point D_1 is affected by the reflected high wave
P_5	The increased pressure at point D_1 is affected by the reflected low wave
ΔU	The drop value of the exit velocity at the peak of the small wave
Δt	The duration of the exit velocity at the peak of the small wave

1 Introduction

Active flow control is a promising method in a wide range of applications (Wang et al. 2013; Xu et al. 2013; Zhang et al. 2018). Recently, as a robust active control device, fluidic oscillator has drawn more and more attention. A fluidic oscillator is a device with no moving parts and capable of generating self-excited and self-sustaining oscillating behavior at the outlet. Fluidic oscillators can generate jets with a wide range of speeds and high frequencies and are resilient to harsh environments. In the year of 2018, the fluidic oscillators were applied in a flight test on a commercial aircraft Boeing 757 (Whalen et al. 2018), demonstrating their robustness in real-world application environments. Therefore, they attracted attention in a wide spectrum of researchers, such as in the rear drag reduction in bluff bodies (Dolgopyat and Seifert 2019; Schmidt et al. 2017), thrust vector control (Raman et al. 2005), cavity noise suppression (Raman and Raghu 2004), flow separation control (Greenblatt et al. 2019; Jentzsch et al. 2019; Whalen et al. 2018), combustion control (Arote et al. 2019; Bohan et al. 2019) and heat transfer enhancement (Mohammadshahi et al. 2020; Kim and Kim 2019). Other active control methods also have obvious advantages and applicable scenarios.

Based on the oscillation mechanisms, Tomac and Gregory (2014) categorized two primary types of oscillators: wall attachment and jet interaction. The wall-attachment oscillators feature internal feedback channels, and operate based on the mechanism of a bi-stable attachment of a jet to adjacent attachment walls through Coanda effect. On the other hand, the jet-interaction oscillators have no feedback channel, but operate based on unsteady interaction of a jet or jets within a cavity that lead to an unsteady external jet. In current study, the wall-attachment oscillators are focused under high-pressure inlet conditions. Based on the internal structures, the wall-attachment oscillators usually have two different configurations. The first type is the sweeping jet oscillator with an internal mixing chamber between two feedback channels (Fig. 1a). In this type of fluid oscillator, the sweeping motion of the jet is controlled by the interaction of the flow in the feedback channel and the recirculating bubbles in the mixing chamber. The main fluid entering the mixing cavity is attracted to the side-wall surface because of the Coanda effect (Coanda 1936; Kourta and Leclerc 2013; Tesař et al. 2013) and closely adheres to the wall surface. The fluid entering the feedback channel acts on the root of the main jet, forcing the main jet to deflect. Therefore, an oscillating jet with a sweep angle of approximately 100° is generated at the exit (Kim et al. 2019). Numerous studies have explored the oscillation mechanisms and parameter optimization of

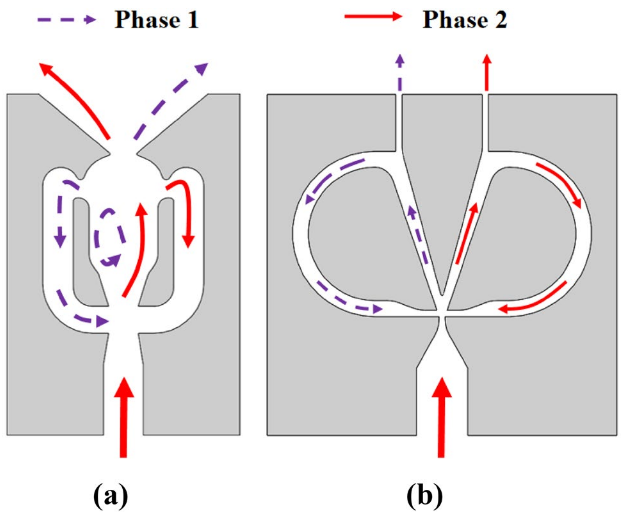

Fig. 1 Two types of fluidic oscillator: **a** sweeping fluidic oscillator, **b** pulse oscillator

these jets (Bobusch et al. 2013a, b; Gaertlein et al. 2014; Ostermann et al. 2015; Raman and Raghu 2004; von Gosen et al. 2015; Wen et al. 2020; Wen et al. 2018; Woszidlo et al. 2015). Bobusch et al. (2013a, b) and Woszidlo et al. (2015) investigated the internal flow dynamics of the sweeping jet oscillator using water as working fluid and particle image velocimetry (PIV) for measurement. A recirculation bubble was found inside the oscillator, which is very helpful in understanding the working mechanism.

The other usual configuration of the wall-attachment oscillator is the "sonic" or pulse oscillator (Fig. 1b). The sonic oscillator has no mixing chamber, but with two discrete outlet channels, which generate anti-phase pulse jets. Unlike the sweeping jet oscillator, the operating frequency of the sonic oscillator is major dependent on the length of the feedback channels. Arwatz et al. (2008) proposed that a pulsed fluidic oscillator could achieve jet pulses with velocity close to that of sound and frequency on the order of several kilohertz. Arwatz et al. (2008) proposed that the oscillation frequency of the oscillator depends on the pressure difference between the two control ports and that between the two branches. Simões et al. (2005) used experimental and numerical methods to study pulse oscillators with liquid and gas media and established a frequency formula with respect to fluid velocity and oscillator size. Wang et al. (2019) established the mechanism and reflection theory of the high pressure compression wave (HPCW) and low pressure expansion wave (LPEW) based on experimental and numerical data of the pressure difference change between two symmetrical points. The main jet deflects to the opposite side under the combined action of the reflecting HPCW and LPEW at the root of the main jet. Yang et al. (2007) added a stepped attachment wall and an acute-angle shunt to the center of the pulsed fluidic oscillator, used particle image velocimetry (PIV) to measure the characteristics of the internal flow field of the oscillator at a low Reynolds number of 3500–45,000, and reported that this design improved the efficiency and stability of the oscillation of the recirculating vortex. Tesař et al. (2013) improved the pulsed fluidic oscillator by leaving one end closed and the other connected to the environment and proposed that the frequency of this oscillator depended on the propagation and reflection of sound waves. Meng et al. (2013) designed a feedback fluid flow meter with a curved connecting wall instead of the traditional straight connecting wall. The results showed that the vibration frequency of the curved-wall feedback flowmeter is greater than that of the straight-wall feedback flowmeter, and the oscillation frequency *f* is only related to the Reynolds number.

In the existing experimental research on fluid oscillators, water was usually used as the working medium under low Re. However, the jet speed and oscillation frequency were relatively limited due to the critical requirement on the water piping system and PIV measurement. It is worth noting that Tomac and Sundström (2019) proposed a feedback-type fluid oscillator design with adjustable frequency at a constant flow rate. Using air as working fluid and a microphone for frequency measurement, they demonstrated that the new design can produce an oscillation frequency more than 10 kHz, which was as high as five times the regular oscillator. In addition, water was also used only for visualization propose.

In current study, air was used as working fluid to facilitate PSP measurement of the fluid dynamics inside the sonic fluid oscillator with kHz oscillation frequency. This work mainly discusses the characteristics of the pulsed fluid oscillator under high pressure. Firstly, a hot wire is used to measure the frequency and velocity characteristics of the oscillator. Then the Kulite high-frequency pressure sensor is used to measure the pressure propagation characteristics of key points, which can be used to explain the frequency characteristics of the oscillator. Then the pressure-sensitive paint (PSP) is used to measure the two-dimensional pressure image. The two-dimensional pressure image is decomposed by the POD method to obtain the modal characteristics, which are used to explain the velocity characteristics of the oscillator.

2 Experimental setup

In this part, the experimental setup is introduced. It mainly includes the design of the oscillator, the test bench and the preparation of the PSP. In current experiment, air was used as working fluid to facilitate the subsonic jet. Together with a hot-wire anemometer and dynamic pressure sensors, mesoporous-particle-based PSP was used to measure the internal flow dynamics.

2.1 Oscillator design

The oscillator model (Fig. 2) had a length of 150.0 mm, a width of 50.0 mm, and a depth of 3.0 mm. The feedback channel width was 2.5 mm, and the outlet width was 1.0 mm. The definition of key points is as follows: point *B* represents the center of the straight channel, point *C* represents the entrance of the feedback channel, point *D* represents the center of the feedback channel, and point *E* represents the exit of the feedback channel. Here, "1" represents the left half of the oscillator and "2" the right half.

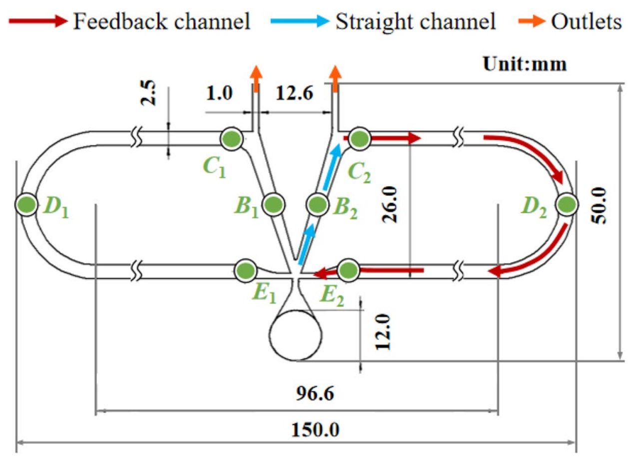

Fig. 2 The internal dimensions of the oscillator

The oscillator model (Figs. 2, 3) included two feedback channels and two outlets, and the length of feedback channel L_f is varied to control the oscillation frequency. To facilitate the measurement of PSP experiment, the oscillator model was divided into two parts. In one part, the oscillator model was made by 3D printing. A 2 mm deep groove was arranged around this part to install cylindrical rubber sealing ring with a diameter of 2.2 mm, avoiding the air leakage. The other part was made by transparent acrylic. The surface of acrylic was smooth and flat. The PSP paint was evenly sprayed on the inner side of the acrylic part. Then, the two parts were fixed with bolts.

2.2 Test bench

As shown in Fig. 3, the test bench included a compressor (Fengbao 265/7, China) providing high-pressure compressed air, a pressure regulator valve (SMC, AW20-02BG, Japan), a mass flow meter (SMC, PFMB7501, Japan), a flow controller, and a pressure gauge (MIK-Y190, China). The hot-wire anemometer adopted the StreamLine Pro CTA system (55P11, Dantec, Danmark), and the calibration velocity range was 8–270 m/s. The sampling frequency of the

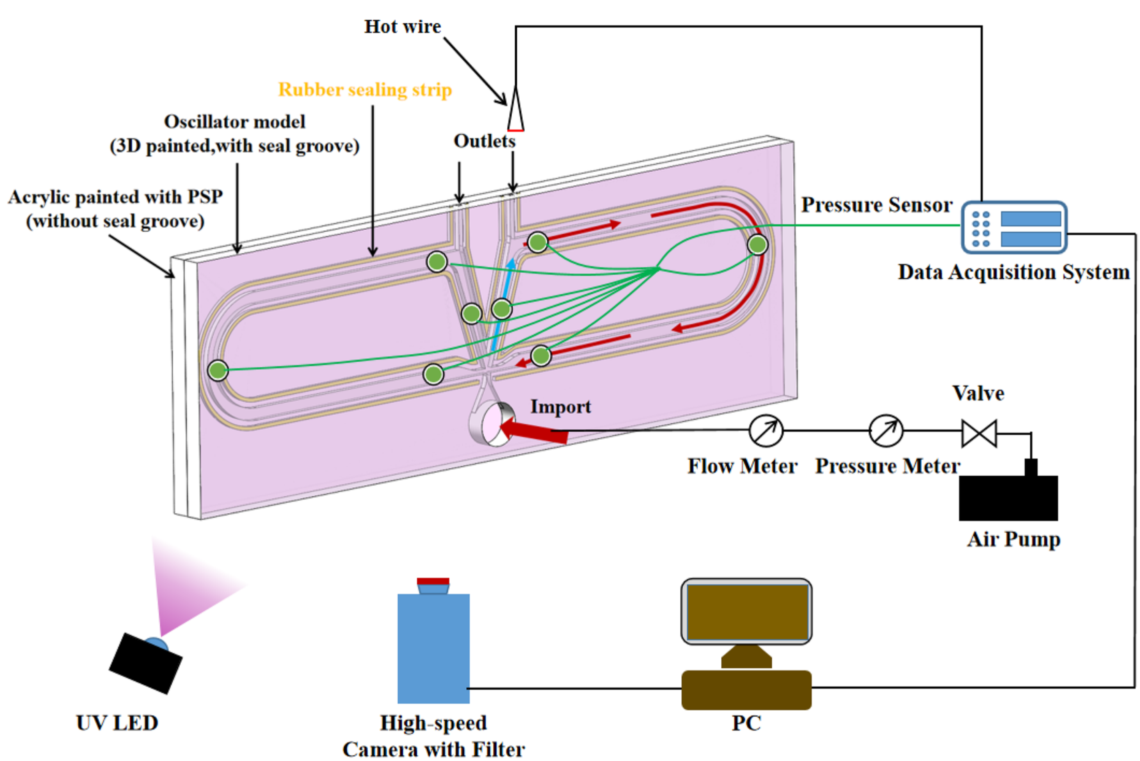

Fig. 3 Test bench

pressure sensor is 200 kHz. To record the change in the exit transient velocity, the data obtained from the hot wire were subjected to temperature correction and fourth-order polynomial curve fitting.

2.3 Fast pressure-sensitive paint

The working medium of the oscillator was high-pressure and high-velocity air. Pressure sensitive paint (PSP) is a promising high-pressure flow field measurement technology that can be used to measure unsteady pressure fluctuations inside the oscillator (Jiao et al. 2018). Gregory et al. (2014) provided a comprehensive review of PSP for flow and acoustic diagnostics.

Of the various types of fast PSP, this study used a novel sprayable fast-responding PSP with mesoporous silicondioxide particles (MP)-PSP (Peng et al. 2018, 2020), which has higher pressure sensitivity, better stability under light, and greater durability while maintaining a similar dynamic response relative to PC-PSP. MP-PSP uses mesoporous and hollow silicon dioxide particles as hosts for luminescent molecules. The MP-PSP paint was prepared according to previous study (Peng et al. 2020): 40 mg polystyrene, 150 mg mesoporous particles (Suzuki Yushi Industrial.) and 1 mg luminophore (PtTFPP, Frontier Scientific) were first added into 1 ml of dichloromethane, and then 1–2% dispersant (Tween 80, Guangdong Runhua Chemistry) was added to the mixture to form a slurry. Ultrasonic treatment was required for 10 min before the paint was evenly sprayed on the acrylic surface. The highly porous and hollow structure of the particles greatly promoted the diffusion of oxygen in the PSP binder. In this experiment, the thickness of the paint was about 20 μm, the step response (90% rise time) of this paint was around 100 μs, resulting in a response frequency of about 10 kHz (Peng et al. 2020). MP-PSP was applied on the acrylic plate, and measurements on the carrier was realized with a back-illumination and imaging setup (Peng et al. 2020).

The PSP was excited using ultraviolet light-emitting diodes with a wavelength of 395 nm (OP-C6U1S-HCI, YueKe Optic, China), and the images were captured using a high-velocity camera (Dimax HS4, PCO AG, Germany) with a 650 ± 25 nm bandpass filter. The excitation wavelength and emission wavelength of MP-PSP paint are 395 nm and 650 nm, respectively. This high-velocity camera had a resolution of 2000 × 2000 pixels. In order to increase the number of images collected in one oscillation period, the image size was truncated to 1500 × 300, and the sampling frequency was set to 15 kHz, thus generating a total of 60,000 images. The experimental setting is shown in Fig. 4. The light intensity of MP-PSP changes according to changes in the pressure. Thus, the alternating light and dark phases in the oscillator channel represent the propagation process of the internal pressure.

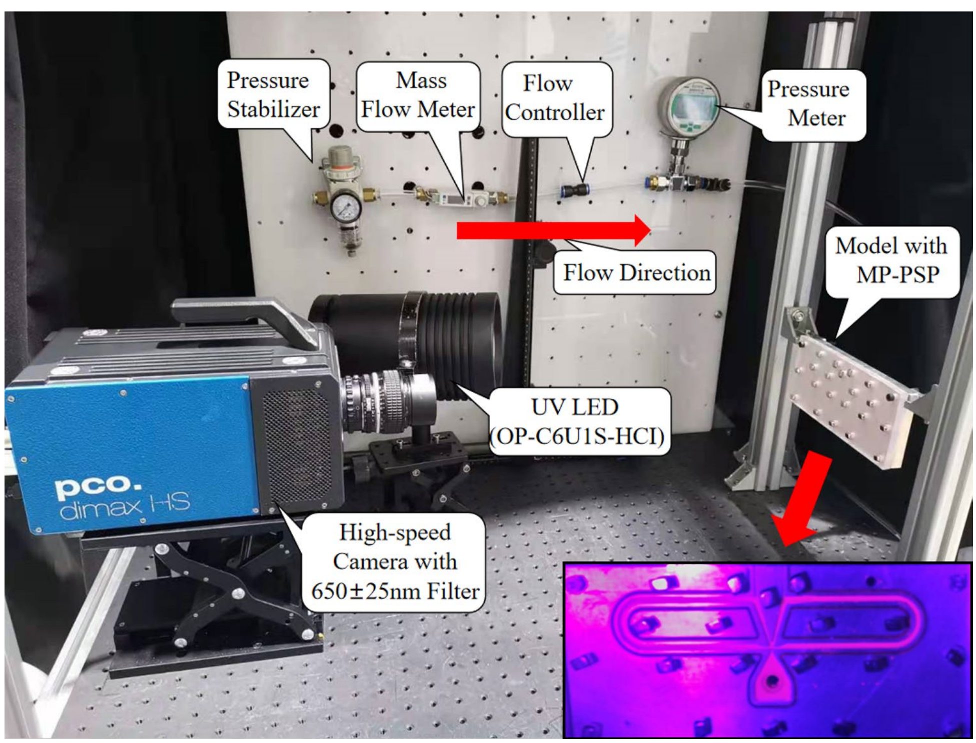

Fig. 4 MP-PSP test bench

2.4 Analysis of uncertainty

For the hot-wire anemometer in the StreamLine Pro CTA system, the frequency characteristic of the anemometer was not added into the uncertainty, when the frequencies in the flow were well below 50% of the cut-off frequency (> 120 kHz for the CTA anemometer). In the calibration, the errors of calibration equipment were stochastic with a normal distribution. The precision of the gage pressure based on Rosemount sensor was 0.5% of max range (600 Pa), the precision of the ambient pressure was 40 Pa, and the precision of the total temperature was 0.5℃. In genial, the relative velocity uncertainty can be summarized in 95% confidence (Perry and Morrison 1971).

The measurement uncertainty of Kulite pressure sensor mainly comes from nonlinear error, hysteresis error and repeatability error. Through the calibration verification of the sensor, it was found that the nonlinearity, hysteresis and repeatability are ± 0.1% FSO BFSL (full scale output best fit straight line) and ± 0.5% FSO BFSL.

The measurement errors of MP-PSP mainly come from pressure sensitivity, temperature dependency, response time, photostability and durability. In the experiment, the spraying thickness of MP-PSP was 20 µm, roughness was 7 µm, pressure sensitivity was 0.75%/kPa, response time (90%) was around 100 µs, temperature dependence was 2.6%/K for 2 µm particles. The pressure sensitivity for the MP-PSP is relatively insensitive to the temperature during the limited temperature change. In the experiment, the temperature error was reduced in the pressure determination based on the alternating current (AC)-coupled method (Crafton et al. 2017; Peng et al. 2018). In the AC-coupled method, the average of wind-on images $I_{on,avg}$ was used as the reference image and the pressure P was determined by:

$$\frac{I_{on,avg}}{I_{on}} = B(T)\frac{P}{P_{avg}} \tag{1}$$

where $B(T)$ was the temperature dependent pressure sensitivity and P_{avg} was the average pressure (can be regarded as the ambient pressure). Because when the pulsed oscillating jet was in stable operation, the ambient temperature and the air temperature in the oscillator remained basically unchanged, so it can be considered that the influence of temperature was very small and can be ignored. Therefore, the temperature error was reduced in the pressure determination based on the AC-coupled method.

3 Data processing method

This part mainly introduces the processing of PSP images and results. It mainly introduces how to process Wind-on and Wind-off images, including image registration, intensity ratio calculation, image repair, modal decomposition and phase average. The POD method and phase averaging are mainly introduced in the process of PSP noise reduction.

3.1 Processing of PSP image

Figure 5 shows the image processing of PSP measurements. The PSP images were post-processed in MATLAB. Image processing mainly included image registration, intensity ratio calculation, image repair, modal decomposition and phase average. Image registration was mainly to solve the slight translation caused by the test process. The calculation and calibration process of the light intensity ratio was as follows: First, several Kulite pressure sensors were installed at the selected key positions of the pulse fluid oscillator, and then the PSP experiment and the pressure sensor experiment were measured simultaneously. During the PSP experiment, only the Wind-on images under UV excitation were taken, and the average value of all Wind-on images was calculated $I_{on,avg}$. According to Eq. 1, the light intensity value was calculated and calibrated with the pressure value.

The 3 × 3 window Gaussian smoothing method was used to process the PSP data. This is because the paint will partially peel off under the impact of high-pressure and high-velocity gas. If it was not processed, it may affect the judgment and interpretation of the results. Local peeling mainly occurred at uneven paint spraying or at corners of the channel. Modal decomposition and reconstruction techniques based on POD were mainly used to extract the dominating pressure dynamics.

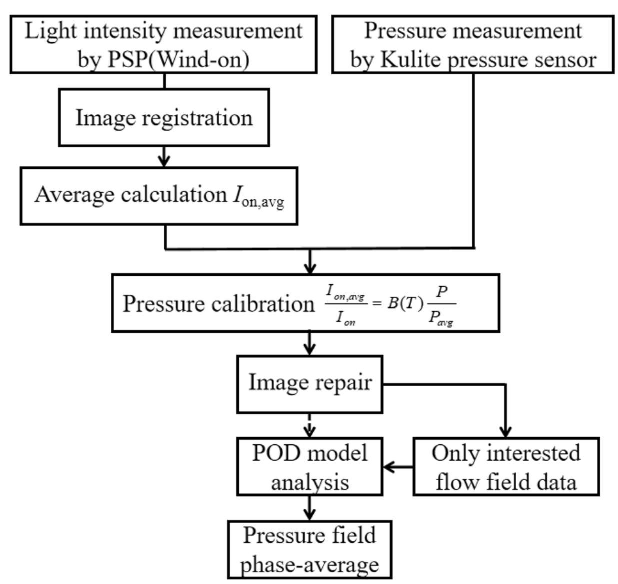

Fig. 5 Processing of PSP image

3.2 POD-based noise reduction method

The basic idea of POD is to establish the time matrix sequence of the PSP pressure fields. Unsteady pressure field U_k can be decomposed through snapshot POD analysis (Sirovich and Kirby 1987):

$$U_k = \tilde{U} + \sum_{i=1}^{N} \phi_i \alpha_i \tag{2}$$

where $\tilde{U}$ is the long-term average field, ϕ_i is the unsteady spatial POD mode, α_i is the corresponding time coefficient, and N is the number of snapshots used in the calculation. To obtain ϕ_i and α_i, the singular value decomposition of the fluctuation field $U_k - \tilde{U}$ is required:

$$\left(\phi, \sqrt{\lambda}, \alpha\right) = \mathrm{svd}(U_k - \tilde{U}) \tag{3}$$

The eigenvalues λ_i represent the fluctuation energy of the spatial POD mode and can be used to sort the POD modes in a descending order. Typically, the energy of the first few modes is much higher than that of the remaining modes, so the entire signal can be characterized using only the first few modes.

In the POD analysis, only the pressure field area in the region of the channels was used, which not only reduced the calculation load, but also eliminated the interference of other unconcerned areas on the analysis process. Firstly, only the data of the pressure field area were extracted and convert them into a column vector. Then, the pressure field areas of all images were converted into column vectors to form a two-dimensional matrix. Finally, spatial POD modes and temporal coefficients were obtained from POD decomposition on this matrix.

According to the energy ratios, dominating POD modes were used for reconstruction by filtering out the background noise modes. Figure 6 shows the effects of POD reconstruction of the PSP results, calibrated by the pressure sensor. In Fig. 6a, the light intensities of the selected pressure points were extracted directly from I_{on}/I_{ref} and compared with the pressure sensors. It can be found that the overall trends for unfiltered PSP agree well with the sensors, except for some pressure peaks. In Fig. 6b, the filtered PSP data by POD reconstruction are highly consistent with the pressure sensor data, by reducing the influence of small disturbances on the overall pressure distribution.

3.3 Phase-averaging process

The fluid has stable periodic uniformity in the oscillator, which necessitates phase analysis of the flow field. Recently, Wen et al. (2020) proposed a phase recognition method based on POD analysis and time-resolved PIV measurement. As shown in Fig. 7, in a similar way, the time coefficients of the first POD mode obtained from PSP measurement inside the oscillator were used for phase identification. After phase identification, at least 100 instantaneous pressure fields within 5° intervals were used to obtain the phase-averaged field. In this way, the averaged pressure fields of 72 phases were obtained. In the transient pressure field before processing, the noise in the measurement area is relatively large, which is mainly caused by camera noise, environmental

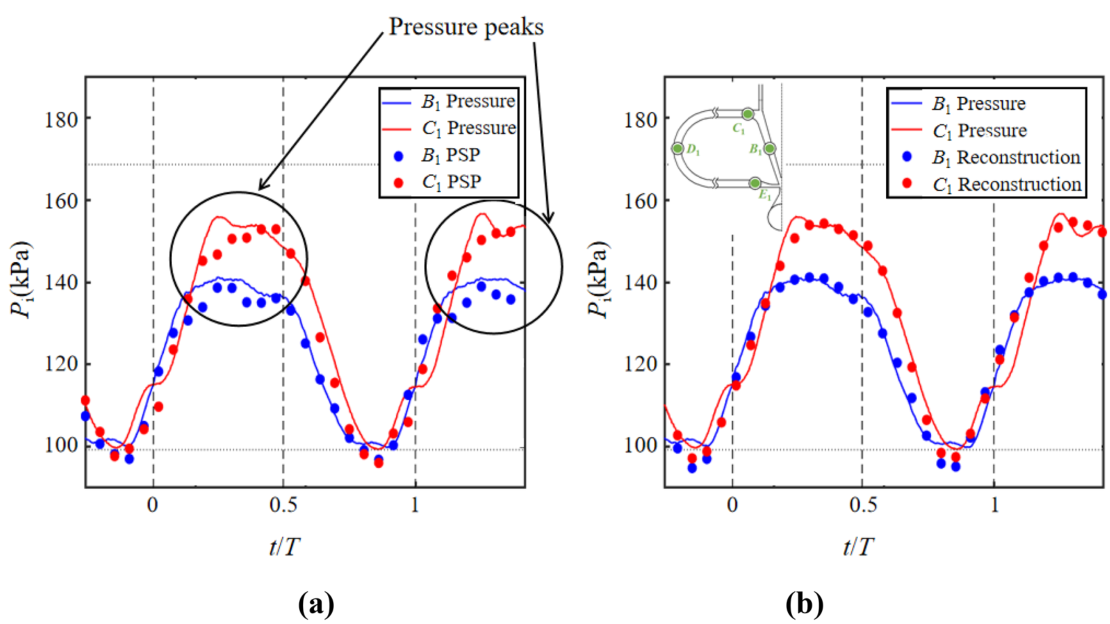

Fig. 6 Comparison of PSP results and pressure sensor data. **a** Unfiltered PSP and **b** filtered PSP by POD reconstruction

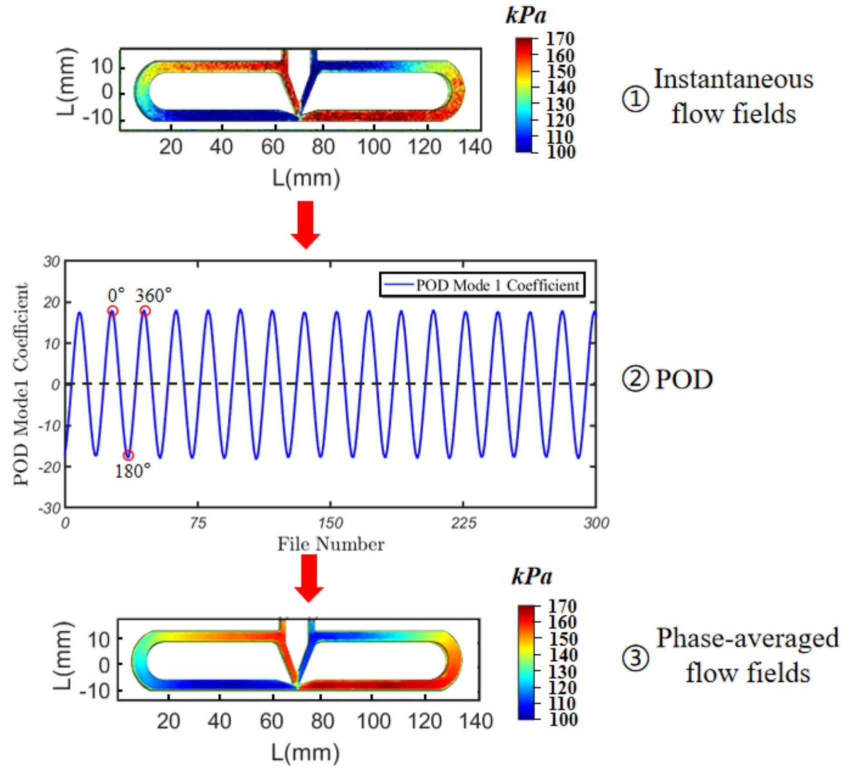

Fig. 7 POD-based phase-averaged pressure field method

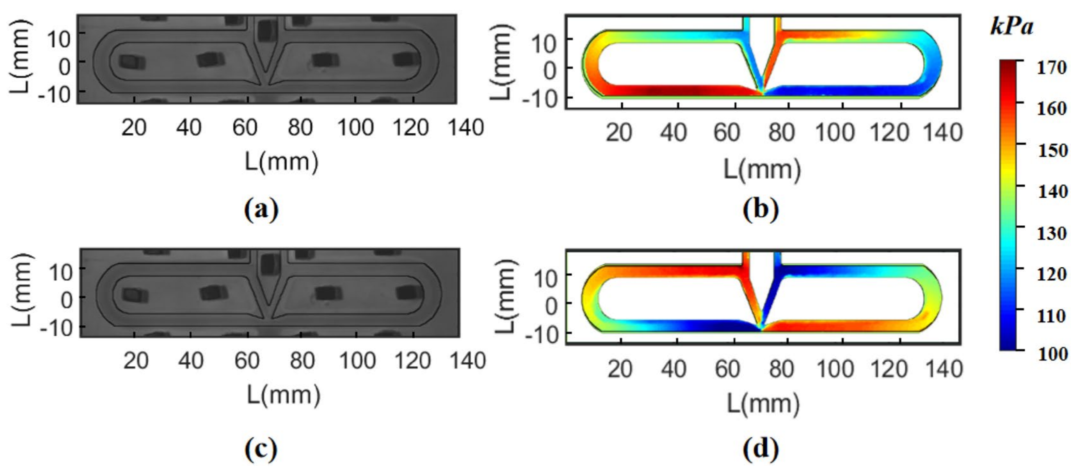

Fig. 8 MP-PSP image processing: **a** Phase 1 wind-on PSP original image, **b** Phase 1 pressure field after image processing, **c** Phase 2 wind-on PSP original image and **d** Phase 2 pressure field after image processing

noise, uneven PSP painting or partial peeling. The quality of the PSP results has been notably improved after phase average process, as shown in Figs. 7 and 8.

Figure 8 shows the PSP Wind-on image before processing and the pressure field after image processing. It can be seen that the quality of the image has been greatly improved. When the oscillator is working, the change in the PSP light intensity was caused by the pressure change in the channel. Through pressure calibration and post-processing, the light intensity value in the oscillator channel can be converted into pressure distribution, as shown in Fig. 8b, d. The black squares in the non-flow field area in Fig. 8a, c are bolts. There is a shadow in a certain area next to the bolt, which is because the ultraviolet lamp used to excite the PSP is working on one side.

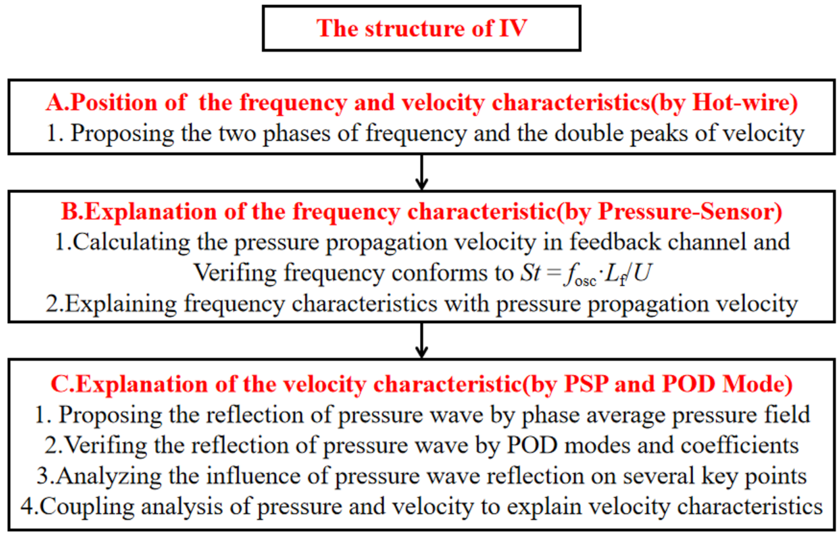

Fig. 9 The structure of Sect. 4

4 Results and discussion

In this part, the operating characteristics of pulsed oscillators under different inlet pressure conditions and feedback channel lengths are discussed. As shown in Fig. 9, in the first step, the external frequency and velocity characteristics of the oscillator obtained from hot wire measurement are discussed. It is found that the frequency trend had two stages and the external velocity has double peaks in the external flow. In the second step, the internal pressure changes at discreate key locations are obtained by Kulite pressure sensors inside the oscillator, providing an explanation of the two stages in frequency trend. In the third step, the two-dimensional pressure dynamics are obtained from PSP inside the oscillator, verifying the pressure wave reflection theory through the POD analysis. At last, the double peaks in the external velocity outside the oscillator are explained by the internal pressure wave reflection. Figure 9 shows the main structure of this chapter.

4.1 Frequency and velocity characteristics of oscillator

Figure 10 shows the frequency characteristics of five oscillators with different feedback channel length (L_f). The frequency characteristics of the experimental data are the same as those in references (Wang et al. 2019). Figure 10a shows that the oscillation frequency decreases as the length of the feedback channel increases. In addition, the frequency characteristics can be divided into two stages. Specifically, up to 1.0 bar, the frequency increases linearly with the inlet pressure, with a relatively steep slope; after 1.0 bar, this slope is less steep. Figure 10b shows that the oscillation frequency has an almost linear relationship with the length of the feedback channel, with negligible difference in the slopes of the

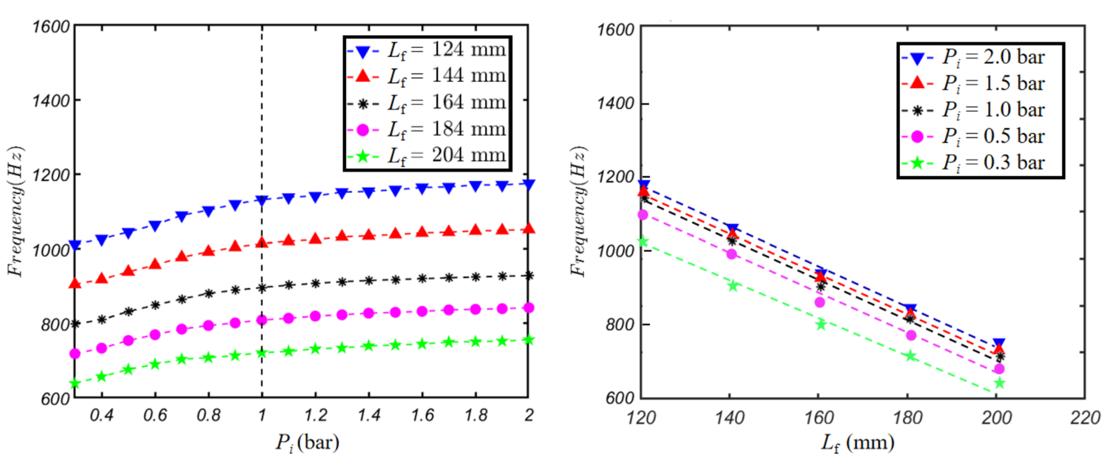

Fig. 10 Frequency characteristics *f* of five oscillators with inlet pressure P_i and feedback channel length (L_f): **a** *f* and P_i and **b** *f* and L_f

curves. The reciprocal of the slope is mainly representative of the change in the propagation velocity of the fluid inside the oscillator (Wang et al. 2016). However, the intercepts of the curves obviously differ, which may represent the effect of the pressure difference in the channels on either side of the oscillator. There is little change in frequency at inlet pressures higher than 1.0 bar, so the region after 1.0 bar is considered the stable working stage.

Figure 11 shows the velocity characteristics of oscillators with two different inlet pressures at feedback channel $L_f = 164$ mm measured by hot-wire anemometer. As the inlet pressure increases, the minimum and maximum outlet velocity also increases. At different inlet pressures, the outlet velocity is relatively stable and presents two peaks in one cycle, as indicated by the circles. As the pressure increases, smaller peaks become more obvious. The multiple peaks during one oscillation cycle of the external velocity indicates that the flow dynamics inside the oscillator not always follow monotonous trend. In order to explain the mechanism of the internal oscillation behaviors, pressure sensor and PSP experiments are also conducted.

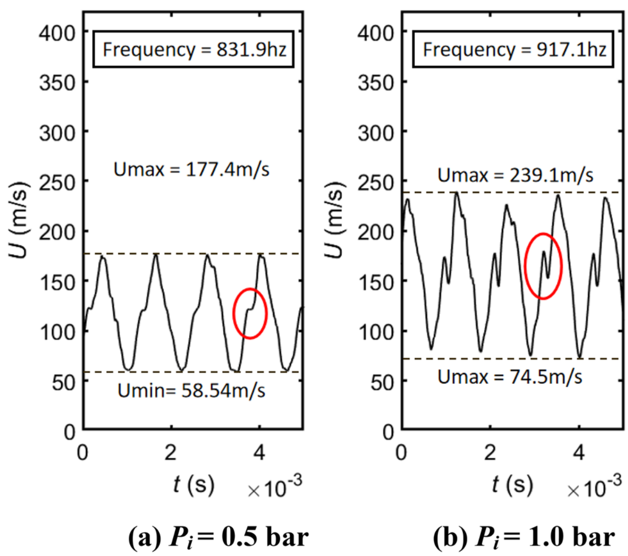

Fig. 11 Velocity characteristics of oscillators with different inlet pressures ($L_f = 164$ mm). **a** $P_i = 0.5$ bar and **b** $P_i = 1.0$ bar

4.2 Explanation of the frequency characteristics of oscillator

This part mainly uses pressure sensor data to explain the frequency characteristics of the oscillator. It is found that the pressure at discrete points changes in a very periodic manner. Therefore, phase averaging and denoising are not required. The pressure data in one oscillation cycle increase sequentially through the feedback channel, and the pressure at different locations are cross correlated in Fig. 12. The pressure at point C_1 is used as the benchmark, and the cross-correlation with D_1, E_1, and C_2 is calculated. The phase differences are 83°, 144°, and 180°, respectively. According to Fig. 10a, the oscillation frequency is 897 Hz when the L_f is 164 mm and the P_i is 1.0 bar. Therefore, the time for the pressure travels from C_1 to E_1 can be determined. Given that $L_{C1E1} = 0.15$ m, the pressure wave traveling speed U_{C1E1} is 334 m/s, which is close to the speed of sound.

In the same way, the pressure wave traveling speeds U_{C1E1} under different inlet pressure P_i are calculated, as shown in Fig. 13. It is found that with the increase of P_i, the trend of U_{CE}/c is divided into two stages, i.e., the linear growth zone and the saturation zone with $U_{CE}/c \approx 1$, where c is the sound speed. Similar to that in Fig. 10a, the two regions are separated by $P_i = 1.0$ bar. According to the explanation of Wang

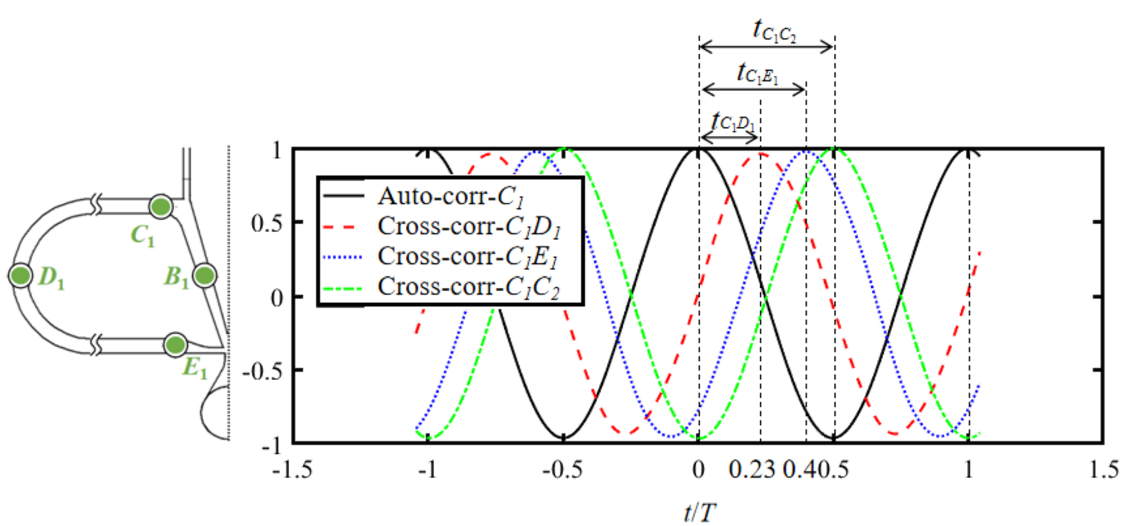

Fig. 12 Cross-correlation calculation of pressure at selected locations ($L_f = 164$ mm, $P_i = 1.0$ bar)

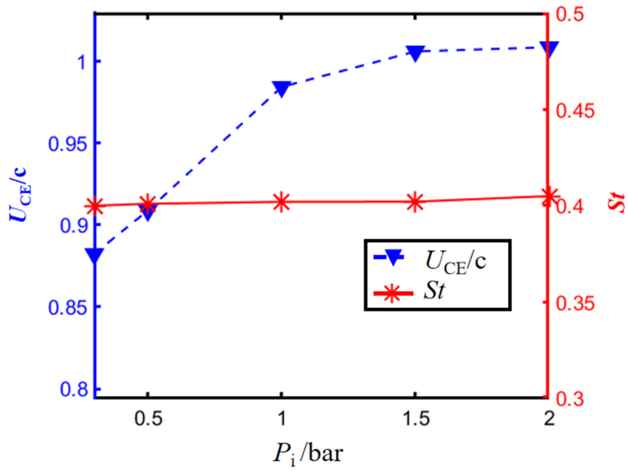

Fig. 13 The relationship between pressure wave traveling speed U_{CE}, Strouhal number St and inlet pressure P_i with feedback channel length of $L_f = 164$ mm. (c is the sound speed)

et al. (2019), the time within a cycle of the pulsed oscillator is mainly related to two parameters, namely the transmission time T_t within the feedback channel and the deflection time T_s. And the deflection time T_s has a much small effect. Therefore, the oscillation frequency is majorly dependent on the transmission time T_t, which can be determined by U_{C1E1}. Therefore, the two-stage characteristics of the oscillation frequency can be explained from the change in the pressure wave speed in the feedback channel. As shown in Fig. 13, U_{CE} increases almost linearly with P_i until P_i reaches 1.0 bar. Accordingly, the oscillation frequency has a linear increasing stage as shown in Fig. 10a. When the P_i has a large value than 1.0 bar, the internal flow velocity is saturated to the sound speed c, due to the "chocking effect" inside the oscillator (Wang et al. 2019). Therefore, the oscillation frequency reaches the saturation zone as shown in Fig. 10a.

Based on the above observation, the non-dimensional Strouhal number is proposed in Eq. 4, defined by the oscillation frequency f, the feedback channel length L_f and the internal pressure wave speed U_{CE}.

$$\mathrm{St} = \frac{fL_f}{U_{CE}} \tag{4}$$

Figure 13 shows the relationship between the St number and the inlet pressure P_i. As the inlet pressure P_i increases, St remains consistent at 0.4. This non-dimensional analysis is helpful in the design and application of the fluidic oscillator.

4.3 Explanation of the velocity characteristics of oscillator

In this part, the two peaks of external velocity are explained by the theory of reflection of pressure waves in the oscillator. Firstly, the pressure wave reflection is revealed from phase-averaged pressure field. Then the pressure wave reflection theory is verified by POD mode and coefficients. Finally, it is found that the reflection of the pressure wave has a great influence on the two peaks of external velocity by coupling the pressure data and the velocity.

4.3.1 Analysis of phase average pressure field

Figure 14 shows the pressure propagation process in a cycle in a pulsed oscillator. The method of phase averaging has been explained in the data processing section. Figure 14a is the pressure diagram at the beginning of the cycle. At this time, high pressure and low pressure begin to be generated in the left and right channels at the same time. Taking the central axis as the dividing line of the flow field, the pressures in the channels on both sides are distributed symmetrically and the pressures are just opposite. In Fig. 14b, the high-pressure wave and the low-pressure wave enter both sides and pass through point C_1. It is shown in Fig. 14c that the front end of the high pressure and low pressure has spread to point D_1. In Fig. 14d, e, the high-pressure and low-pressure waves continue to propagate forward and reach point E_1. In Fig. 14f, the pressure at point E_1 continues to rise, and the pressure at point E_2 continues to drop. In the first half of the cycle, the pressure distribution in the oscillator is consistent with expectations and high pressure and low pressure only propagate forward.

A strange phenomenon is found in Fig. 14g. The high pressure area in the pressure channel on the left has begun to accumulate, because the high pressure area has passed through point D_1 to point E_1. The pressure at point D_1 was expected to gradually drop. However, at point D_1, the pressure further increases instead. And, the area near D_1 became a high-pressure zone again, which was called pressure wave reflection in Wang et al. (2019). The left channel in Fig. 14h is still affected by this high-pressure reflection, but the pressure in the high-pressure zone gradually decreases.

Comparing Fig. 14f, g, it is proposed that the high-pressure wave has pressure reflection. When the high pressure reaches the root of the main jet along the feedback channel, a part of the pressure is reflected back and propagated in the reverse direction.

4.3.2 Analysis of POD modes and coefficients

To further verify the pressure wave reflection phenomenon, the POD mode and temporal coefficients are analyzed below

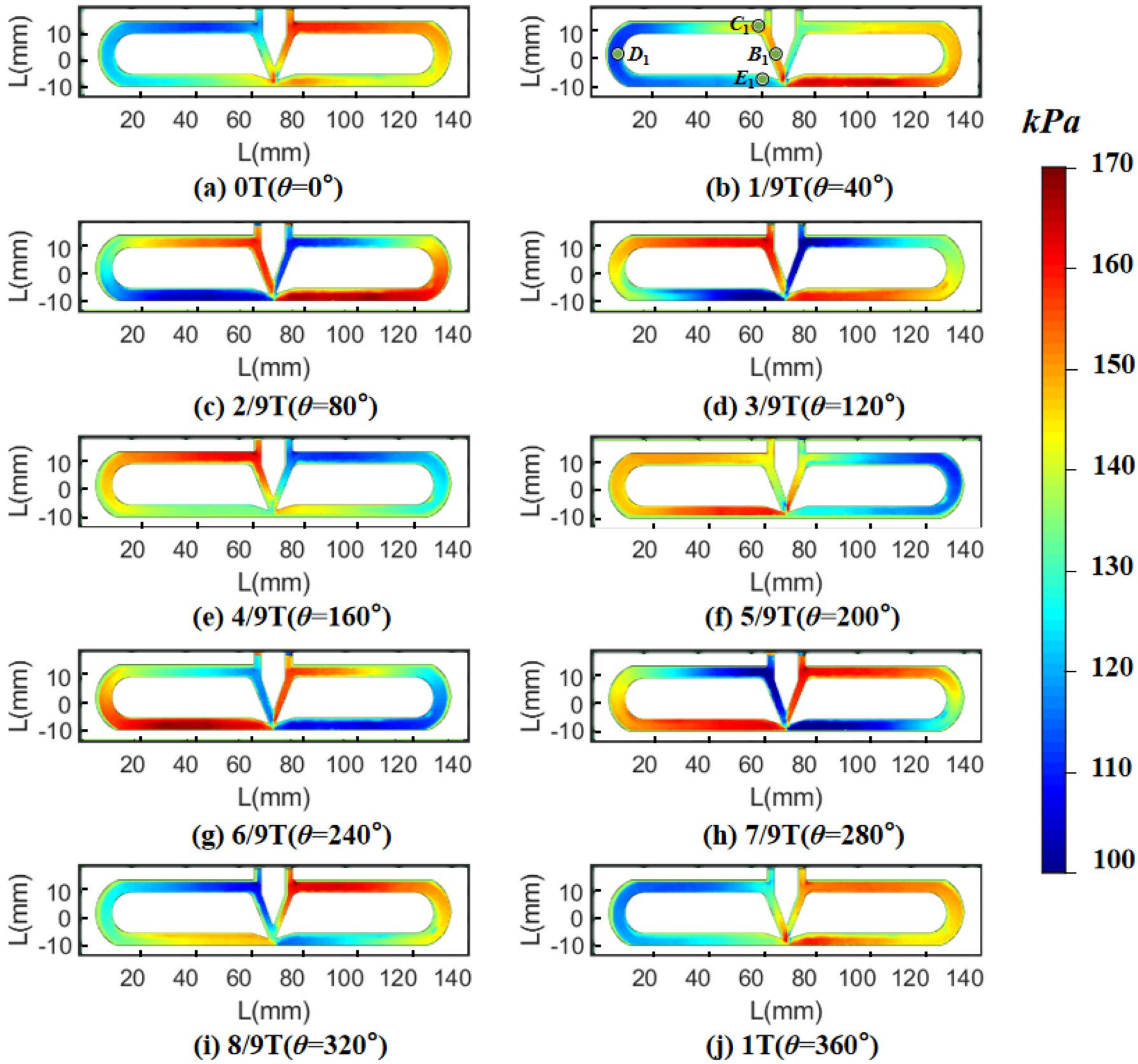

Fig. 14 Phase average flow field display of different phases ($L_f = 164$ mm, $P_i = 1.0$ bar)

to provide a more in-depth explanation. After the images are decomposed by POD, the POD spatial mode and temporal coefficients are obtained, and the temporal coefficients are Fourier transformed. There are 10,000 POD coefficients when the Fourier calculation is performed. The sampling frequency is 15 kHz, and window is not used in the Fourier calculation.

Figure 15 calculates the energy ratio of the POD modes and the frequency of the temporal coefficients. In Fig. 15a, the first 6 modes account for 95% of the total energy, which means that the first 6 modes can capture the major flow dynamics. Among them, mode 1 accounts for about 63% of the total energy, mode 2 for about 30%, and modes 3–6 for about 2%. In Fig. 15b, Fourier transform is performed on the temporal coefficients of the first 6 modes. The coefficient peak frequencies of mode 1 and mode 2 are consistent with the oscillator operating frequency. The peak coefficient frequencies of modes 3–6 are multiple times of the operating frequency, i.e., twice for mode 3, three times for modes 4 and mode 6, four times for mode 5, respectively.

The frequency of the first six modal coefficients seems to have a great relationship with the operating frequency. To clearly explain this phenomenon, it is necessary to analyze the POD mode. The modes mainly capture pressure fluctuations at different regions. The transient pressure fields with different phases can be reconstructed by the modes and temporal coefficients. It is shown in Fig. 16 that the pressure fluctuation of mode 1 majorly happens in the second half of the feedback channel. Mode 2 mainly reflects the pressure fluctuation in the first half of the feedback channel. The frequencies of mode 1 and mode 2 are consistent with the operating frequency, which means that mode 1 and mode 2 can mainly reflect the main propagation of pressure inside the oscillator.

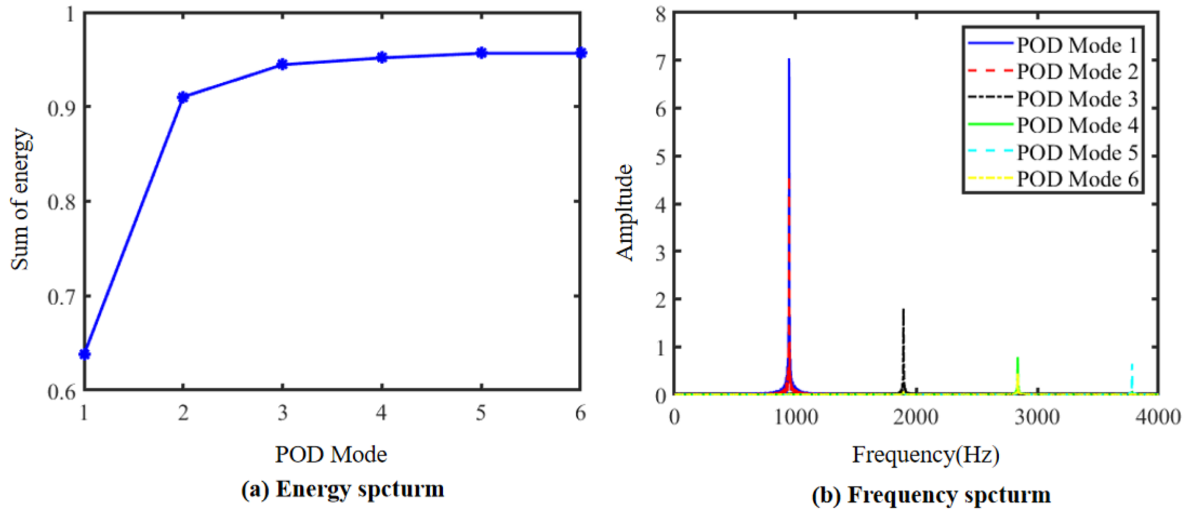

Fig. 15 POD coefficient energy and frequency ($L_f = 164$ mm, $P_i = 1.0$ bar)

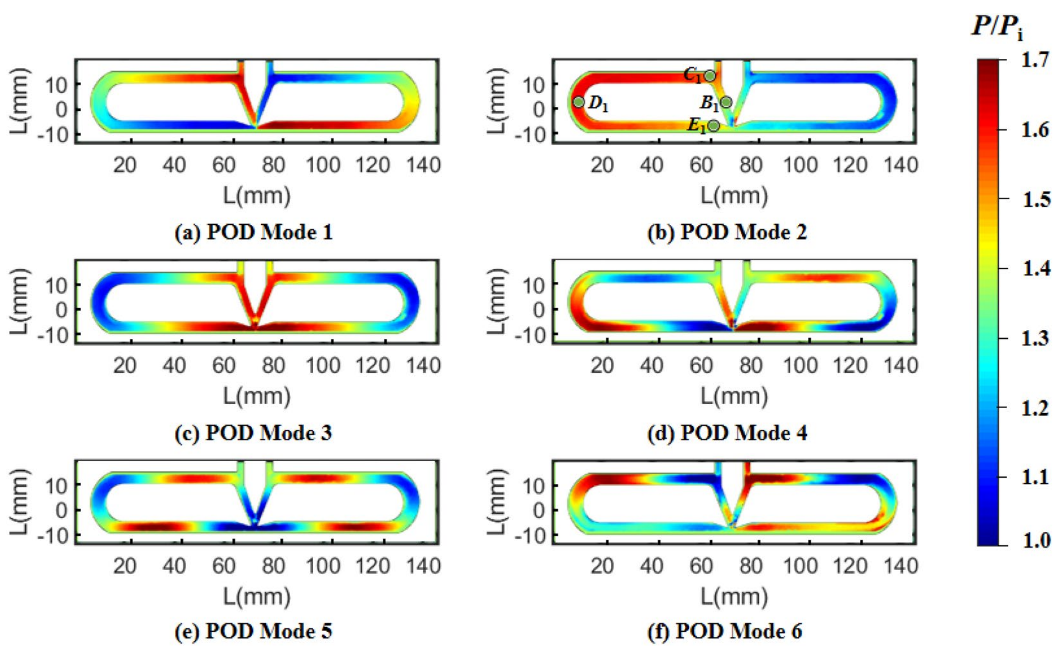

Fig. 16 POD modes ($L_f = 164$ mm, $P_i = 1.0$ bar)

In mode 3, the pressure fluctuations are mainly concentrated in the channels on both sides of the split wedge, and the pressure on both sides of the split wedge changes simultaneously. This is because the main jet deflection occurs twice in a cycle. When the main jet is deflected, the front end of the high pressure is transmitted to one side, and there is residual high pressure on the other side to propagate. Therefore, mode 3 mainly reflects the pressure changes in the channels on both sides of the split wedge.

Mode 4 mainly reflects the pressure fluctuations at the ends of the feedback channel, especially the pressure changes at points E_1 and D_1. The frequency of the mode coefficient of mode 4 is 3 times of the operating frequency, which means that the pressure at E_1 and D_1 increases 3 times in one cycle. In one cycle, when high pressure enters the feedback channel to propagate, the pressure increases once at E_1 and D_1. When the low pressure propagates in the feedback channel, it will squeeze the high pressure wave ahead, and the pressure will increase once again at E_1 and D_1. When the front end of the high-pressure wave reaches the root of the main jet, the reflected high-pressure wave propagates in the feedback channel in the reverse direction, and the

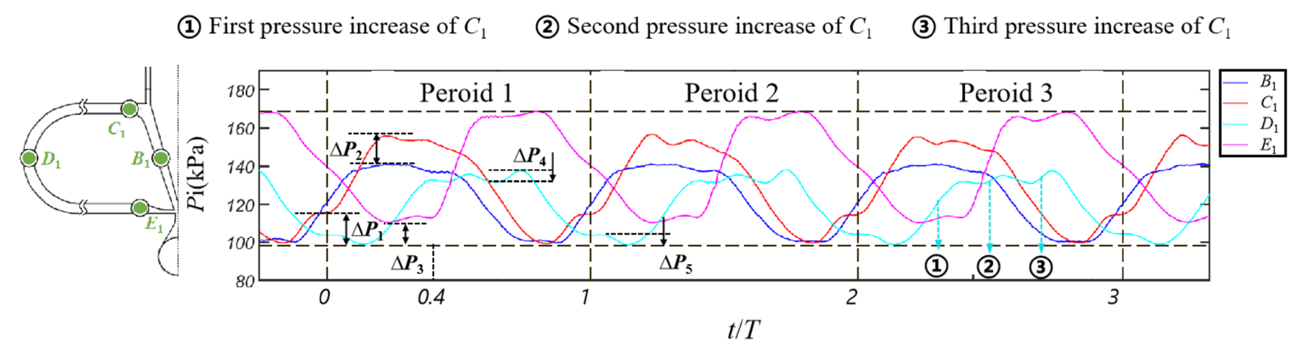

Fig. 17 The pressure propagation process in three oscillation cycles ($L_f = 164$ mm, $P_i = 1.0$ bar)

pressure increases once again at E_1 and D_1. The frequency of mode 6 is also 3 times of the operating frequency, but with a phase lag to mode 4. The multiple oscillation frequencies in the pressure dynamics inside the oscillator are confirmed by the discrete pressure sensors (see Fig. 17).

Through the analysis of modal and modal coefficients, it is verified that there is high-voltage wave reflection in the feedback channel. And POD mode 4 and mode 6 show the dynamics of the reflected wave.

4.3.3 Analysis of pressure and velocity coupling

This part mainly analyzes the influence of the pressure reflection inside the feedback channel on the external velocity.

In Fig. 17, the starting point of the oscillation period is defined when the pressure at point C_1 starts to rise from a plateau stage, i.e., $t/T = 0$. It is found that when the pressure at point B_1 and point C_1 both reach the maximum, the pressure at point C_1 is higher than that at point B_1 by ΔP_2. There is a period of pressure increase at point C_1 before the start of the cycle, i.e., $t/T = 0$. During this period of time, the pressure at point C_1 is always higher than that at point B_1, and then the pressure at point C_1 remains unchanged for a short period of time in the plateau stage. The rising pressure at point C_1 during this period is defined as ΔP_1. It is found that ΔP_1 and ΔP_2 are equal. Obviously, ΔP_2 is rooted from ΔP_1. In addition, the sum of ΔP_3 and ΔP_4 is found to be equal to ΔP_1 in Fig. 17. Here ΔP_3 is the difference between the lowest pressure at point E_1 and atmospheric pressure, i.e., 100 kPa. ΔP_4 is the fluctuation pressure at point D_1. From the analysis in Sect. 4.3.1, ΔP_3 and ΔP_4 can be defined as the pressure increase in the channel caused by the reflected pressure wave. ΔP_5 is the pressure drop at point D_1 caused by the reflection of the low-pressure wave. Besides, the pressure at point D_1 has three small peaks in the plateau, which is consistent with the results in the frequency spectrum of POD mode 4 (in Fig. 15), verifying the pressure wave reflection.

Figure 18 shows the coupled analysis of the internal reflected pressure wave and external velocity. Point C_1 and point B_1 are selected due to their close locations to the exit. In Fig. 18a, b, the Area 1 is defined by the difference between the pressure at point C_1 and point B_1, and the reflected pressure wave is defined as ΔP_1. In Fig. 18c, d, the velocity decrease and duration of the secondary peak in the external jet velocity are defined as ΔU and Δt, respectively. In Fig. 18a, b, the pressure at point C_1 increases with the inlet pressure P_i, caused by the reflected high-pressure wave, resulting in a larger Area 1. Because point C_1 is located at the junction of the inlet of the feedback channel and the oscillator exit, the pressure fluctuation at point C_1 will inevitably affect the external jet velocity. Accordingly, in Fig. 18c, d, the secondary peak in the external velocity is also enlarged with the increase in the inlet pressure P_i, resulting in larger ΔU and Δt. Therefore, a close correlation between the internal pressure and external velocity is found. The secondary peak of the external velocity is close related to the propagation of the reflected pressure wave as well as the inlet pressure P_i.

5 Conclusion

This article focuses on analyzing the frequency and velocity characteristics of a subsonic oscillator by PSP image and pressure sensors data. The following are the conclusions of this article:

1. The frequency of the oscillator has two stages with the increase in inlet pressure, i.e., linear growth stage and saturation stage. The two stages of frequency are explained by calculating the pressure wave speed using internal pressure sensors in the oscillator feedback channel. The internal pressure wave speed increases with the inlet pressure until it reaches a saturation value of sound speed. Based on that, the Strouhal number St is defined by the feedback channel length and pressure wave speed.

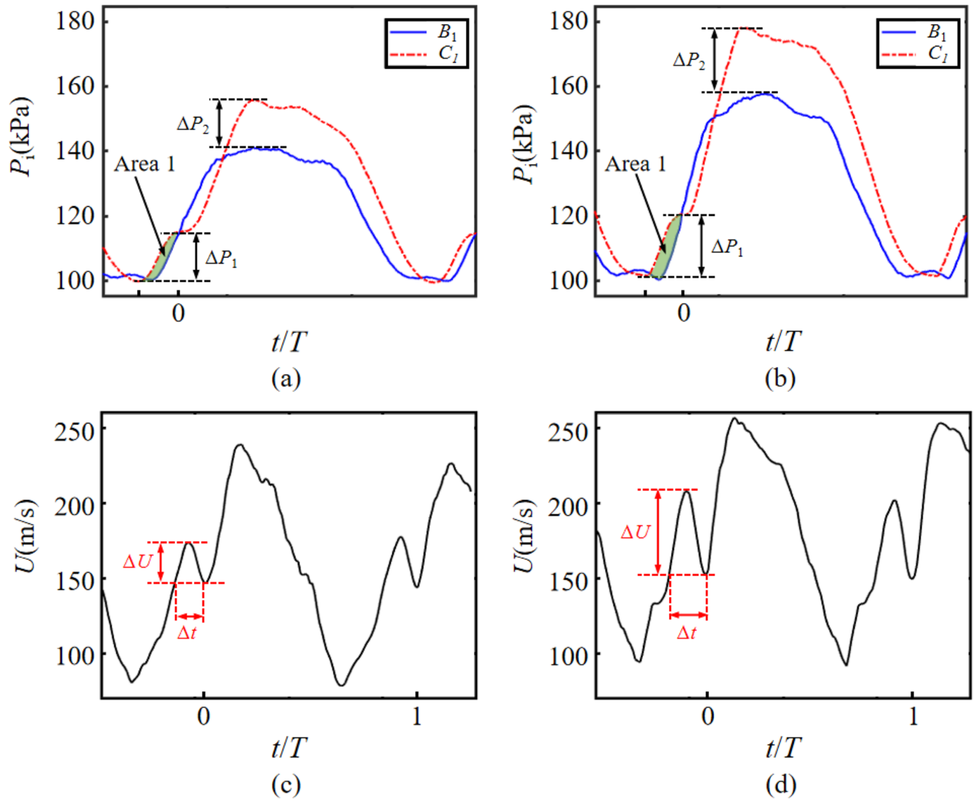

Fig. 18 Coupling analysis of internal pressure and external velocity ($L_f = 164$ mm). **a** Pressure propagation ($P_i = 1.0$ bar), **b** pressure propagation ($P_i = 1.5$ bar), **c** velocity characteristics ($P_i = 1.0$ bar) and **d** velocity characteristics ($P_i = 1.5$ bar)

As such, the St has a constant value of 0.4 under current working conditions with different inlet pressure and feedback channel length.

2. The external jet velocity of the oscillator presents a double peak phenomenon, and the scale of the wavelet peak increases with the inlet pressure. The generation of the wavelet peak is related to the reflection of the high-pressure wave in the oscillator. The PSP results reveal that the high-pressure wave propagating in the feedback channel will be reflected back after it touches the end of the feedback channel. The reflected pressure wave causes fluctuations in the feedback channel, resulting the wavelet peak in the external jet velocity. The higher the inlet pressure, the large the wavelet peak.

Dynamic pressure fields obtained with PSP are used to explain the internal flow mechanism of the oscillator. The paper provides guidance for the design of fluidic oscillators for various applications.

Acknowledgements The authors gratefully acknowledge the financial support from the National Natural Science Foundation of China (12072196), Advanced Jet Propulsion Innovation Center (AEAC HKCX2019-01-016; HKCX2020-02-028), Aero-engine Foundation (6141B09050399), Science and Technology Commission of Shanghai Municipality (19JC1412900) and the Oceanic Interdisciplinary Program of Shanghai Jiao Tong University (SL2020MS006) extended to this study.

References

Arote A, Bade M, Banerjee J (2019) Numerical investigations on stability of the spatially oscillating planar two-phase liquid jet in a quiescent atmosphere. Phys Fluids 31(11):112103. https://doi.org/10.1063/1.5123762

Arwatz G, Fono I, Seifert A (2008) Suction and oscillatory blowing actuator. In: IUTAM symposium on flow control and MEMS (IUTAM Bookseries). Springer, Dordrecht, pp 33–44. https://doi.org/10.1007/978-1-4020-6858-4_4

Bobusch B, Woszidlo R, Bergada J, Nayeri C, Paschereit C (2013a) Experimental study of the internal flow structures inside a fluidic oscillator. Exp Fluids 54(6):1–12. https://doi.org/10.1007/s00348-013-1559-6

Bobusch BC, Woszidlo R, Krüger O, Paschereit CO (2013) Numerical investigations on geometric parameters affecting the oscillation properties of a fluidic oscillator. In: 21st AIAA computational fluid dynamics conference, p 2709. https://doi.org/10.2514/6.2013-2709

Bohan B, Polanka M, Rutledge J (2019) Sweeping jets issuing from the face of a backward-facing step. J Fluids Eng 141(12):121201. https://doi.org/10.1115/1.4043576

Coanda H (1936) Device for deflecting a stream of elastic fluid projected into an elastic fluid. United States Patent 2(052):869

Crafton JW, Gregory J, Sellers M, Ruyten W (2017) Data processing tools for dynamic pressure-sensitive paint. In: 55th AIAA aerospace sciences meeting. https://doi.org/10.2514/6.2017-0701

Dolgopyat D, Seifert A (2019) Active flow control virtual maneuvering system applied to conventional airfoil. AIAA J 57(1):72–89. https://doi.org/10.2514/1.J056258

Gaertlein S, Woszidlo R, Ostermann F, Nayeri C, Paschereit CO (2014) The time-resolved internal and external flow field

properties of a fluidic oscillator. In: 52nd Aerospace sciences meeting, p 1143. https://doi.org/10.2514/6.2014-1143
Gosen F, Ostermann F, Woszidlo R, Nayeri CN, Paschereit CO (2015) Experimental investigation of compressibility effects in a fluidic oscillator. In: 53rd AIAA aerospace sciences meeting, AIAA 2015-0782. https://doi.org/10.2514/6.2015-0782
Greenblatt D, Whalen E, Wygnanski I (2019) Introduction to the flow control virtual collection. AIAA J 57(8):3111–3114. https://doi.org/10.2514/1.J058507
Gregory J, Sakaue H, Liu T, Sullivan J (2014) Fast pressure-sensitive paint for flow and acoustic diagnostics. Ann Rev Fluid Mech 46(1):303–330. https://doi.org/10.1146/annurev-fluid-010313-141304
Jentzsch M, Taubert L, Wygnanski I (2019) Using sweeping jets to trim and control a tailless aircraft model. AIAA J 57(6):2322–2334. https://doi.org/10.2514/1.J056962
Jiao L, Peng D, Wen X, Liu Y, Gregory JW (2018). Experimental study of the interaction between rotor wake and a cylinder in hover. In: Applied aerodynamics conference, AIAA 2018-4214. https://doi.org/10.2514/6.2018-4214
Kim S, Kim H, Kim K (2019) Measurement of two-dimensional heat transfer and flow characteristics of an impinging sweeping jet. Int J Heat Mass Transf 136:415–426. https://doi.org/10.1016/j.ijheatmasstransfer.2019.03.021
Kim S, Kim H (2019) Quantitative visualization of the three-dimensional flow structures of a sweeping jet. J vis 22(3):437–447. https://doi.org/10.1007/s12650-018-00546-1
Kourta A, Leclerc C (2013) Characterization of synthetic jet actuation with application to Ahmed body wake. Sens Actuators A Phys 192:13–26. https://doi.org/10.1016/j.sna.2012.12.008
Meng X, Xu C, Yu H (2013) Feedback fluidic flowmeters with curved attachment walls. Flow Meas Instrum 30:154–159. https://doi.org/10.1016/j.flowmeasinst.2013.02.006
Mohammadshahi S, Samsam-Khayani H, Nematollahi O, Kim KC (2020) Flow characteristics of a wall attaching oscillating jet over single-wall and double-wall geometries. Exp Therm Fluid Sci 112:110009. https://doi.org/10.1016/j.expthermflusci.2019.110009
Ostermann F, Woszidlo R, Nayeri C, Paschereit C O (2015) Experimental comparison between the flow field of two common fluidic oscillator designs. In: 53rd AIAA aerospace sciences meeting, AIAA 2015-0781. https://doi.org/10.2514/6.2015-0781
Peng D, Gu F, Li Y, Liu Y (2018) A novel sprayable fast-responding pressure-sensitive paint based on mesoporous silicone dioxide particles. Sens Actuators A Phys 279:390–398. https://doi.org/10.1016/j.sna.2018.06.048
Peng D, Xie F, Liu X, Lin J, Li Y, Zhong J, Zhang Q, Liu Y (2020) Experimental study on hypersonic shock–body interaction between bodies in close proximity using translucent fast pressure- and temperature-sensitive paints. Exp Fluids 61(5):1–18. https://doi.org/10.1007/s00348-020-02948-0
Perry AE, Morrison GL (1971) A study of the constant-temperature hot-wire anemometer. J Fluid Mech 47(3):577–599. https://doi.org/10.1017/S0022112071001241
Raman G, Packiarajan S, Papadopoulos G, Weissman C, Raghu S (2005) Jet thrust vectoring using a miniature fluidic oscillator. Aeronaut J 109(1093):129–138. https://doi.org/10.1017/S0001924000000634
Raman G, Raghu S (2004) Cavity resonance suppression using miniature fluidic oscillators. AIAA J 42(12):2608–2612. https://doi.org/10.2514/1.521
Schmidt H, Woszidlo R, Nayeri C, Paschereі C (2017) Separation control with fluidic oscillators in water. Exp Fluids 58(8):1–17. https://doi.org/10.1007/s00348-017-2392-0
Simões E, Furlan R, Bruzetti Leminski R, Gongora-Rubio M, Pereira M, Morimoto N, Santiago Avilés J (2005) Microfluidic oscillator for gas flow control and measurement. Flow Meas Instrum 16(1):7–12. https://doi.org/10.1016/j.flowmeasinst.2004.11.001
Sirovich L, Kirby M (1987) Low-dimensional procedure for the characterization of human faces. J Opt Soc Am A Opt Image Sci Vis 4(3):519–524. https://doi.org/10.1364/josaa.4.000519
Tesař V, Zhong S, Rasheed F (2013) New fluidic-oscillator concept for flow separation control. AIAA J 51(2):397–405. https://doi.org/10.2514/1.J051791
Tomac M, Gregory J (2014) Internal jet interactions in a fluidic oscillator at low flow rate. Exp Fluids 55(5):1–14. https://doi.org/10.1007/s00348-014-1730-8
Tomac M, Sundström E (2019) Adjustable frequency fluidic oscillator with supermode frequency. AIAA J 57(8):3349–3359. https://doi.org/10.2514/1.J058301
Wang J, Choi K, Feng L, Jukes T, Whalley R (2013) Recent developments in DBD plasma flow control. Prog Aerosp Sci 62:52–78. https://doi.org/10.1016/j.paerosci.2013.05.003
Wang S, Baldas L, Colin S, Orieux S, Kourta A, Mazellier N (2016) Experimental and numerical study of the frequency response of a fluidic oscillator for active flow control. In: 8th AIAA flow control conference, AIAA 2016-4234. https://doi.org/10.2514/6.2016-4234
Wang S, Batikh A, Baldas L, Kourta A, Mazellier N, Colin S, Orieux S (2019) On the modelling of the switching mechanisms of a Coanda fluidic oscillator. Sens Actuators A Phys 299:111618. https://doi.org/10.1016/j.sna.2019.111618
Wen X, Li Z, Zhou L, Yu C, Muhammad Z, Liu Y, Wang S, Liu Y (2020) Flow dynamics of a fluidic oscillator with internal geometry variations. Phys Fluids 32(7):075111. https://doi.org/10.1063/5.0012471
Wen X, Liu Y, Tang H (2018) Unsteady behavior of a sweeping impinging jet: time-resolved particle image velocimetry measurements. Exp Therm Fluid Sci 96:111–127. https://doi.org/10.1016/j.expthermflusci.2018.02.033
Whalen E, Shmilovich A, Spoor M, Tran J, Vijgen P, Lin J, Andino M (2018) Flight test of an active flow control enhanced vertical tail. AIAA J 56(9):3393–3398. https://doi.org/10.2514/1.J056959
Woszidlo R, Ostermann F, Nayeri C, Paschereit C (2015) The time-resolved natural flow field of a fluidic oscillator. Exp Fluids 56(6):1–12. https://doi.org/10.1007/s00348-015-1993-8
Xu Y, Feng L, Wang J (2013) Experimental investigation of a synthetic jet impinging on a fixed wall. Exp Fluids 54(5):1–13. https://doi.org/10.1007/s00348-013-1512-8
Yang J, Chen C, Tsai K, Lin W, Sheen H (2007) A novel fluidic oscillator incorporating step-shaped attachment walls. Sens Actuators A Phys 135(2):476–483. https://doi.org/10.1016/j.sna.2006.09.016
Zhang B, Liu K, Zhou Y, To S, Tu J (2018) Active drag reduction of a high-drag Ahmed body based on steady blowing. J Fluid Mech 856:351–396. https://doi.org/10.1017/jfm.2018.703